Ionization and Energy Loss Beyond Perturbation Theory

P. L. Grande[1] and G. Schiwietz[2]

[1] *Instituto de Física da Universidade Federal do Rio Grande do Sul, Avendida Bento Gonçalves 9500, 91501-970, Porto Alegre, Brazil*
[2] *Bereich SF, Hahn-Meitner-Institut Berlin, Glienicker Str. 100, D-14109 Berlin, Germany*

Abstract

A review is given on the application of the coupled-channel method for the calculation of the electronic energy loss of ions as well as ionization in matter. This first principle calculation, based on the solution of the time-dependent Schrödinger equation, has been applied to evaluate the impact parameter and angular dependence of the electronic and nuclear energy losses of ions as well as the ionization due to high-power short laser pulses. The results are compared to experimental data as well as to other current theoretical models.

Contents

1. Introduction 8
2. The coupled-channel method 9
   2.1. Impact-parameter method 9
   2.2. Independent particle model 11
   2.3. Wave functions – the basis set 13
   2.4. Matrix elements 16
   2.5. Ionization/stopping/straggling cross sections 18
      2.5.1. Electronic 18
      2.5.2. Nuclear 20
   2.6. Two-center calculations 23
3. Higher order effects 24
4. Photon vs. charged-particle ionization 29
5. Comparison with measurements 33
   5.1. Gas targets 33
      5.1.1. Angular dependence 33
      5.1.2. Stopping cross section 35
   5.2. Solid targets 38
6. Simple models for the energy loss 39
7. What have we learned from coupled-channel calculations 42
Acknowledgements 43
References 44

ADVANCES IN QUANTUM CHEMISTRY, VOLUME 45
ISSN: 0065-3276 DOI 10.1016/S0065-3276(04)45002-3

1. INTRODUCTION

The electronic energy loss has been studied for many years because of its direct application in problems concerning material damage and ion beam analysis. The theoretical treatment of the energy loss in atomic collisions has been greatly improved over the last decades and relies on an accurate treatment of target-continuum states up to high-emitted electron energies. Calculations of the electronic energy loss have been performed by using traditional methods known from atomic physics investigations such as the plane wave Born approximation (PWBA) [1,2], the high-energy solution by Bethe [3] and the semi-classical approximation (SCA) [4]. More advanced models are the Continuum-Distorted Wave Eikonal-Initial-State (CDW-EIS) [5], the classical trajectory Monte Carlo (CTMC) [6,7], the ACAM-CKLT model based on Liouville and Wigner equations in phase space [8], the Electron Nuclear dynamics (END) [9] and finally the atomic orbital coupled-channel method (AO) [10–13] that yields reliable values for the impact-parameter dependent electronic energy loss. These methods based on atomic physics calculations offer reliable ways to obtain detailed information on the energy-loss processes in gases as well as for the inner-shell electrons of solids. Of course, other approaches have to be adopted for conduction-band electrons of solid-state targets [14–17] in order to obtain an accurate description of the energy loss due to the valence electrons. Other models such as those of Refs. [18–21] have strongly enlarged our understanding of the physical processes that govern the energy loss.

In recent years we have investigated the electronic energy loss of bare and screened ions for light targets using the coupled-channel method. This first principle calculation [10–12], based on an expansion of the time dependent electronic wave function in terms of atomic orbitals, has been successfully applied to evaluate the impact-parameter and angular dependence of the electronic energy loss and the total stopping cross section of ions (antiprotons, H and He) colliding with H and He atoms at energies of 1–500 keV/amu. It has also been applied to calculate the entrance-angle dependence of the stopping force for He ions channeling along the Si main crystal directions [22,23] as well the shape of the surface peak for protons backscattered from Al under channeling and blocking conditions [24].

These benchmark calculations have also been used to check simplified models that account for the basic energy loss processes without the need of large scale calculations [25,26] and to calculate the probability of multiphoton ionization in the case of intense fs-laser pulses [27].

The chapter is organized as follows. The principle of the coupled-channel method is reviewed in detail in Section 2. The results are discussed in connection to higher order terms in Section 3. The application to multiphoton ionization is described in Section 4. Comparisons with measurements are provided in Section 5. A simple model for the electronic energy loss is

presented and compared to coupled-channel calculations in Section 6 and finally the conclusion and outlook are presented in Section 7. If not indicated otherwise, atomic units ($e = m = \hbar = 1$) will be used throughout the chapter.

2. THE COUPLED-CHANNEL METHOD

Here we will focus the attention on atomic treatments of the energy-transfer process. Thus, we will not consider solid-state effects such as intra-band transitions, collective excitations (bulk and surface plasmons) and the corresponding dynamic projectile screening.

Generally, ion–atom collision processes may be described either by first- or second-order perturbative approaches or by coupled-channel calculations. Perturbation theory often yields simple and in some cases even analytical results, but has the disadvantage of being valid only for high incident energies and low projectile charge states. In this work we will use the highest-order (coupled-channel) theory, which allows for an infinite number of interactions between projectile, target, and electron. The electron may be ionized in the first step and may be accelerated or decelerated in the second step. It is also possible that an electron, after being ionized, is 'thrown' back to the initial state. Furthermore, the probability for ionizing an electron is always less than or equal to unity. All this does not hold for perturbation theory. In the following, the basic ingredients of our model will be described.

2.1. Impact-parameter method

The theoretical formulation of atomic excitation and ionization processes is conveniently discussed by introducing the quantum-mechanical Hamilton operator. For a three-body system the Hamiltonian reads

$$\mathcal{H} = T_{\mathrm{p}}(\vec{r}_{\mathrm{p}}) + T_{\mathrm{t}}(\vec{r}_{\mathrm{t}}) + T_{\mathrm{e}}(\vec{r}_{\mathrm{e}}) + V_{\mathrm{pt}}(\vec{R}) + V_{\mathrm{te}}(\vec{r}) + V_{\mathrm{pe}}(\vec{R} - \vec{r}) \qquad (1)$$

with the kinetic and potential energies denoted by T and V, respectively. The subscripts 'p', 't', and 'e' refer to the projectile ion, target core, and electron as indicated in Fig. 1. In the following we will use the impact-parameter method, i.e., it is assumed that $\vec{r}_{\mathrm{p}}$ and $\vec{r}_{\mathrm{t}}$ are given by classical paths $\vec{r}_{\mathrm{p}} = \vec{r}_{\mathrm{p}}(t, b)$, $\vec{r}_{\mathrm{t}} = \vec{r}_{\mathrm{t}}(t, b)$ (determined by the impact parameter b). This concept was first introduced by Bang and Hansteen [28]. It is well known [29] that the impact-parameter methods are valid as long as the Coulomb parameter

$$\nu_{\mathrm{i}\to\mathrm{f}} = \frac{Z_{\mathrm{p}} Z_{\mathrm{t}}}{q_{\mathrm{i}\to\mathrm{f}}} \approx \frac{Z_{\mathrm{p}} Z_{\mathrm{t}} v_{\mathrm{p}} m_{\mathrm{p}}}{\Delta E_{\mathrm{i}\to\mathrm{f}}} \qquad (2)$$

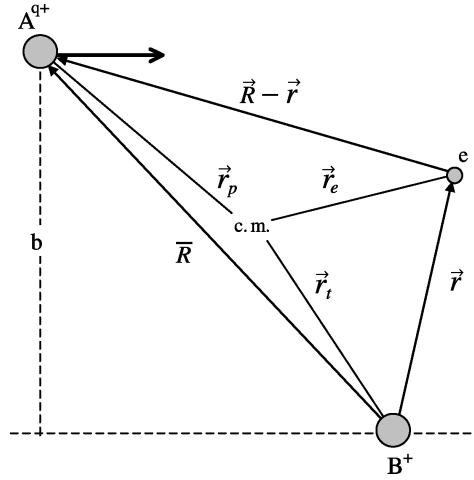

Fig. 1. Vector diagram for the projectile ion A^{q+}. the ionic target core B^+, and one active electron. The impact parameter b is indicated. $\vec{r}_p$, $\vec{r}_t$ and $\vec{r}_e$ are position vectors of projectile, target, and electron in the center-of-mass system.

is large compared to unit ($q_{i\to f}$ is the momentum transfer). This is always valid if the incident ion has at least thermal energies. If, additionally, an independent motion of the electron [30] is assumed, one may solve the time-dependent Schrödinger equation for one active electron:

$$\left(\mathrm{i}\frac{\partial}{\partial t} - \mathcal{H}_\mathrm{e}\right)\Phi_\mathrm{e}(t) = 0 \tag{3}$$

with

$$\mathcal{H}_\mathrm{e}(t) = \mathcal{H}_\mathrm{te} + V_\mathrm{pe}(\vec{R}(t) - \vec{r}) \tag{4}$$

and

$$\mathcal{H}_\mathrm{te}(t) = T_\mathrm{e}(\vec{r}_\mathrm{e}) + V_\mathrm{te}(\vec{r}_\mathrm{e} - \vec{r}_\mathrm{t}(t)). \tag{5}$$

In the subsequent treatment the electron coordinate will be measured from the accelerated target nucleus and is the only dynamical variable. Thus the target system is the frame of reference [31,32]. In such a noninertial system non-Newtonian forces arise. The corresponding Hamiltonian $\mathcal{H}_\mathrm{te}$ is

$$\mathcal{H}_\mathrm{te} = -V_\mathrm{te}(\vec{r}) + T_\mathrm{e}(\vec{r}) + V_\mathrm{recoil}(\vec{r}, \vec{r}_\mathrm{t}(t)). \tag{6}$$

It is reasonable to neglect the last term V_recoil. By doing this transitions are excluded which are due to the interaction of the active electron with the recoiling target nucleus. This so-called recoil effect leads to insignificant contributions to total cross sections, but may be important for very close collisions ($b < 10^{-3}$ a.u.) [33]. Before the solution of equation (3) is

explained in detail, the classical path $\vec{R}(t)$ should be defined. Given the time-dependent electronic wave function Φ_e, a classical Hamiltonian for the heavy particles may be defined:

$$\mathcal{H}_h = T_p(\vec{r}_p) + T_t(\vec{r}_t) + V_{pt}(\vec{R}) + \langle \Phi_e | V_{pe}(\vec{R} - \vec{r}) | \Phi_e \rangle + \langle \Phi_e | V_{te}(\vec{r}) | \Phi_e \rangle. \quad (7)$$

With this Hamiltonian the classical equations of motion are solved. The last term in equation (7) was neglected because of its small influence on the motion of the target core in case of a strongly target-centered wave function Φ_e. It is emphasized that the concept defined by equation (7) introduces for the first time a dynamically curved projectile trajectory in the impact-parameter method. Thus the projectile motion is coupled to the motion of the active electron. However, since the projectile interacts with a mean electronic field, there is only approximate conservation of energy and momentum. For small projectile scattering angles this deficiency can be circumvented. In this case conservation of energy and momentum may be forced by applying the Eikonal transformation [34].

It is noted that some calculations have been performed with hyperbolic projectile paths. In this case only the first three terms in equation (7) are considered. However, most of the previous calculations have been performed for straight line paths, as given by the first two terms in equation (7). Such calculations are equivalent to quantum-mechanical solutions of the three-body Schrödinger equation with plane projectile waves. Typical examples for such quantum-mechanical three-body theories are the plane-wave Born approximation [35] and its limiting form at high incident energies, the Bethe theory [36]. However, the main advantage of the present model compared to previous stopping-power theories is the highest-order (coupled-channel) description of the electronic motion.

2.2. Independent particle model

The electronic many-body Hamiltonian in equation (1) is treated in the framework of the independent-electron frozen-core model. This means that there is only one active electron, whereas the other electrons are passive (no dynamic correlation is accounted for) and no relaxation occurs. In this model the electron–electron interaction is replaced by an initial-state Hartree–Fock–Slater potential [37]. This treatment is expected to be highly accurate for heavy collision systems at intermediate to high incident energies. The largest uncertainties of the independent-electron model will show up for low-Z few-electron systems, such as $H^0 + H^0$ and $H + He^0$ or for high multiple-ionization probabilities.

The independent-electron approximation allows for a distinction of target electrons and projectile-centered electrons which screen the projectile

nuclear charge. One of the most important dynamic correlation effects (deviations from the independent-electron approximation) is the collision of a target electron with a projectile-centered electron [38,39]. This will directly enhance the energy loss and reduce the projectile screening. It follows that a separate treatment of the different projectile charge states is important for reliable predictions of the mean energy loss for atomic targets [4,10,11,40], insulators and at higher incident energies also for metals [41].

The time-dependent Schrödinger equation may be solved by expanding $\Phi_e(\{\vec{r}\},t)$ in terms of unperturbed eigenfunctions φ_i of the target with coefficients $a_i(t) = \langle\varphi_i|\Phi_e(t)\rangle$. Thus, equation (3) is replaced by a set of coupled first-order differential equations, the so-called coupled-channel equations

$$\mathrm{i}\frac{\mathrm{d}}{\mathrm{d}t}a_i(t) = \sum_j a_j(t)\mathrm{e}^{\mathrm{i}(E_i-E_j)t}V_{j\to i}(\vec{R}(t)) \tag{8}$$

with the internuclear distance $\vec{R}$ and

$$V_{j\to i}(\vec{R}(t)) = \langle\varphi_i|V_{\mathrm{pe}}(\vec{R}(t),\vec{r})|\varphi_j\rangle. \tag{9}$$

E_i is the orbital energy associated with the target wave function φ_i. Here V_{pe} is an effective potential seen by the active electron, which contains the screening effect produced by other electrons from the medium. For bare incident ions, the active-electron projectile interaction V_{pe} is just the Coulomb potential. However, in the case where the projectile carries electrons, we use a screened potential made up of the Coulomb part due to the projectile-nuclear charge and the static potential produced by the target electrons that screen the projectile-nuclear charge

$$V_{\mathrm{pe}}(\vec{R}-\vec{r}) = -\frac{Z_{\mathrm{p}}}{|\vec{R}-\vec{r}|} + \sum_n^{\mathcal{N}}\int \mathrm{d}^3r'\frac{|\chi_n(\vec{r}')|^2}{|\vec{R}-\vec{r}-\vec{r}'|}, \tag{10}$$

where Z_{p} is the projectile nuclear charge, χ_n is the projectile-electron wave function and $\mathcal{N}$ is the number of projectile electrons. The wave functions χ_n for each electron n of the projectile are obtained according to the Hartree–Fock–Slater procedure [37]. Thus, we neglect dynamic screening (a time dependence of χ_n due to target induced polarization, respectively, excitation/ionization), Pauli correlation (anti-symmetrization of the projectile- and target-centered wave functions) as well as dynamic correlation effects due to the residual electron–electron interaction. It is pointed out, that the dynamic electron–electron interaction is not included in the present model since there is only one active electron.

For high projectile speeds and low projectile charge-states the transition matrix elements $V_{j\to i}$ are small. This is the domain of first-order perturbation theory (SCA, first-order Born approximation). In this case, most transitions

are governed by the direct step from the initial state j to the final i. Thus, we may drop the summation over j and use $a_j(t) = 1$ (the state j corresponds to the ground state). Hence, the time-consuming solution of the coupled-channel equations is reduced to a set of simple integrals over time within perturbation theory.

2.3. Wave functions – the basis set

The starting point of the present theory is an expansion of the time-dependent electronic wave function Φ_e in terms of single-center eigenfunctions φ_i of the target Hamiltonian $\mathcal{H}_{te}$

$$\Phi_e(\vec{r}, t) = \Phi_B(\vec{r}, t) + \Phi_C(\vec{r}, t), \tag{11}$$

$$\Phi_B(\vec{r}, t) = \sum_{n,l,m} a_{n,l,m}(t) e^{-iE_{n,l}t} \varphi_{n,l,m}(\vec{r}), \tag{12}$$

$$\Phi_C(\vec{r}, t) = \sum_{l,m} \int_0^\infty d\varepsilon \, b_{n,l,m}(\varepsilon, t) e^{-i\varepsilon t} \varphi_{\varepsilon,l,m}(\vec{r}). \tag{13}$$

In the above equations n, l and m are the main quantum number and the quantum numbers associated with angular momentum and angular momentum projection, respectively. The eigenfunction $\varphi_{n,l,m}(\vec{r})$ is defined in the usual way as

$$\varphi_{n,l,m}(\vec{r}) = \frac{1}{r} u_{n,l}(r) Y_{l,m}(\Omega) \tag{14}$$

and

$$E_{n,l} u_{n,l}(r) = \left(-\frac{d^2}{2\, dr^2} + \frac{l(l+1)}{2r^2} - V_t(r) \right) u_{n,l}(r), \tag{15}$$

where $E_{n,l}$ and the subscript n have to be replaced by ε for continuum states. The radial wave functions $u_{n,l}$ and $u_{\varepsilon,l}$ are calculated numerically using a Runge–Kutta method with variable step width. The bound-state wave functions $u_{n,l}$ are integrated from large r values down to zero and free wave functions are calculated from zero towards large r in order to suppress any irregular component in the wave function. The numerical uncertainty of the bound-state eigenvalues $E_{n,l}$ is about 10^{-6}. Boundary values for small r are obtained from a polynomial expansion of V_{te} and $u_{\varepsilon,l}$. The normalization of continuum states is similar to the method described by Cowan [42]. Bound-state wave functions are dimensionless whereas the continuum states are normalized per square root of energy (in a.u.). Hence it follows from equation (13) that the coefficients $b_{l,m}$ are also given per square root of energy (in a.u.). The eigenfunctions of $\mathcal{H}_{te}$ should be complete and

orthogonal. The completeness was checked by calculating the overlap matrix elements between an arbitrary target-centered wave function and Φ_e. The sum over the corresponding squared overlap matrix elements was equal to unity to within 10^{-4}. Orthogonality was verified by calculating overlap matrix elements between different eigenfunctions φ_i which are typically in the order of 10^{-5}. The infinite sums in equations (12) and (13) have to be truncated in order to perform the numerical calculation of the time-dependent wave function or the corresponding coefficients a and b. This introduces no problems for the bound states since highly excited states are generally less populated than the K, L or M shell. However, electrons captured into projectile states, as well as high-energy continuum electrons, lead to a population of high l states of target-centered wave functions. Thus partial waves exceeding orbital angular momenta of $l = 8$ often have to be considered for the continuum states. Another problem arises since the continuous energy variable of the free wave functions is not easy to handle in a numerical calculation. Therefore, the continuum is represented by a sum over a few (about 10 for each orbital angular momentum in the present work) pseudodiscrete radial wave functions $\Psi_{l,m}$:

$$\Phi_C(\vec{r},t) = \sum_{j,l,m} \frac{1}{r}\,\Psi_{l,m}(\varepsilon_j - \Delta\varepsilon_j/2, \varepsilon_j + \Delta\varepsilon_j/2, r, t) Y_{l,m}(\Omega), \qquad (16)$$

$$\Psi_{l,m}(E_1, E_2, r, t) = \int_{E_1}^{E_2} \mathrm{d}\varepsilon\; b_{l,m}(\varepsilon, t) \mathrm{e}^{-\mathrm{i}\varepsilon t} u_{\varepsilon,l}(r). \qquad (17)$$

An exact solution for $\Psi_{l,m}$ may be given in case of a pulse-like ionization process at $t = 0$. The corresponding moving wave packet is known as a Weyl packet [43,44],

$$\Psi_{l,m}(E_1, E_2, r, t) \approx \bar{b}_{l,m}(\bar{\varepsilon}, t) \int_{E_1}^{E_2} \mathrm{d}\varepsilon\; \mathrm{e}^{-\mathrm{i}\varepsilon t} u_{\varepsilon,l}(r). \qquad (18)$$

However, the numerical treatment of such explicitly time-dependent basis states would be time consuming compared to the treatment of bound states. Thus we search for a further simplification of $\Psi_{l,m}$ by investigating the asymptotic behavior of Coulomb wave functions [42]. For $r\Delta\varepsilon \ll \pi$ the radial wave function $u_{\varepsilon,l}$ is nearly independent of ε and may be considered constant for integration. For $\varepsilon t \ll \pi$ the exponential function in equation (18) is nearly independent of ε. In both cases $\Psi_{l,m}$ in equation (18) may be replaced by

$$\Psi_{l,m}(E_1, E_2, r, t) \approx \frac{\bar{b}_{l,m}(\bar{\varepsilon}, t)}{E_2 - E_1} \left(\int_{E_1}^{E_2} \mathrm{d}\varepsilon\; \mathrm{e}^{-\mathrm{i}\varepsilon t} \right) \left(\int_{E_1}^{E_2} \mathrm{d}\varepsilon\; u_{\varepsilon,l}(r) \right) \qquad (19)$$

$$\begin{aligned}\Psi_{l,m}(E_1,E_2,r,t) &= \bar{b}_{l,m}(\bar{\varepsilon},t)\mathrm{e}^{-\mathrm{i}\bar{\varepsilon}t}F(E_2-E_1,t)\int_{E_1}^{E_2}\mathrm{d}\varepsilon\, u_{\varepsilon,l}(r)\\ &= \frac{\bar{a}_{l,m}(\bar{\varepsilon},t)}{\sqrt{E_2-E_1}}\mathrm{e}^{-\mathrm{i}\bar{\varepsilon}t}F(E_2-E_1,t)\int_{E_1}^{E_2}\mathrm{d}\varepsilon\, u_{\varepsilon,l}(r),\end{aligned} \tag{20}$$

with

$$F(\Delta E,t) \equiv \frac{2}{t\Delta E}\sin\left(\frac{t\Delta E}{2}\right). \tag{21}$$

The dimensionless coefficients $\bar{a}$ correspond to the coefficients $\bar{b}$ defined above. Except for $\bar{a}$ and the exponential function in equation (19), all quantities are real numbers and only the integral over the radial continuum wave functions needs to be calculated numerically. A damping function similar to F was introduced by Reading *et al.* [44] in order to improve the asymptotic behavior of continuum wave functions. However, the wave packets as described above are only approximate solutions for large values of t and r. It is evident that this deficiency will affect mainly those continuum states which have a considerable overlap with asymptotic projectile states. Most of these states are neglected anyway because of the finite number of target-centered partial waves ($l < 11$) taken into account. From the structure of Coulomb wave functions it is obvious that transition matrix elements involving either a high Rydberg state or a low-energy continuum state are identical when re-normalized per square root of energy [42]. Since an explicit summation over an infinite number of bound states is impossible in a numerical treatment, we have integrated these re-normalized Rydberg wave functions up to the continuum threshold. The resulting Rydberg wave packet is then added to the lowest energy continuum packet. In this way approximate completeness of the basis set is achieved.

It is noted that other authors have either neglected the damping factor F [29,43] or they used only approximate atomic wave functions in similar descriptions of the electronic motion.

From symmetry properties of the wave function and from the Coulomb matrix elements it is possible to distinguish between two classes of basis states, namely gerade (denoted by $+$) and ungerade (denoted by $-$) states. The corresponding wave functions Φ^+ and Φ^- may be obtained by replacing the spherical harmonics $Y_{l,m}$ in equation (14) by

$$Y^{\pm}_{l,|m|} = \frac{1}{\sqrt{2}}(Y_{l,|m|} \pm (-1)^m Y_{l,-|m|}), \tag{22}$$

for $m \neq 0$ and

$$Y^{+}_{l,0} = Y_{l,0}. \tag{23}$$

The projectile interaction does not lead to transitions between gerade and ungerade states. Therefore, only states with the same symmetry as the ground state have to be considered. The coupled-channel equations are solved in the present work for about 500 gerade states (including to up 50 bound states), which replace about 900 eigenstates. The gerade (or ungerade) states are chosen to yield optimum convergence for a certain regime of incident energies.

2.4. Matrix elements

In order to integrate the coupled-channel equation (8) the time as well as the impact-parameter dependence of the matrix elements (equation (9)) have to be determined. For this purpose, the matrix elements $V_{j\to i}(\vec{R}(t))$ are expanded in terms of the radial (R) and angular ($\hat{R}$) parts of the internuclear vector $\vec{R}$ according to

$$V_{j\to i}(\vec{R}(t)) = -\sum_{L=|l_i-l_j|}^{l_i+l_j} W_{L,M}^{i,j} G_L^{i,j}(R) Y_{L,M}(\hat{R}), \qquad M = m_j - m_i, \tag{24}$$

which is obtained after separating the radial and angular parts (determined by the spherical harmonics $Y_{L,M}$) of the atomic target wave function φ_i. The coefficients $W_{L,M}^{i,j}$ are given by

$$W_{L,M}^{i,j} = \left(\frac{4\pi(2l_i+1)(2l_j+1)}{2L+1}\right)^{1/2} (-1)^{m_i+M} \begin{pmatrix} l_i & l_j & L \\ 0 & 0 & 0 \end{pmatrix} \times \begin{pmatrix} l_i & l_j & L \\ -m_i & m_j & -M \end{pmatrix}. \tag{25}$$

The symbols

$$\begin{pmatrix} \cdots & \cdots & \cdots \\ \cdots & \cdots & \cdots \end{pmatrix}$$

in equation (25) represent the Wigner '3j' symbol as described in Ref. [45]. We consider only screened interaction potentials, which are spherically symmetric. In this case the function $G_L^{i,j}(R)$ can be written as

$$G_L^{i,j}(R) = \int_0^\infty \mathrm{d}r u_i^* u_j f_L(r,R), \tag{26}$$

where u_i, u_j are the radial wave functions of the states i and j, respectively. The function $f_L(r,R)$ is determined by the interaction potential and is given

by

$$f_L(r,R) = -Z_p \frac{r_<^L}{r_>^{L+1}}, \tag{27}$$

for the Coulomb potential $-Z_p/(|\vec{R}-\vec{r}|)$ and

$$f_L(r,R) = \lambda(2L+1)(-1)^L A_L(\lambda r_<) H_L(\lambda r_>). \tag{28}$$

for the Bohr-like screened potential

$$\frac{\exp(-\lambda|\vec{R}-\vec{r}|)}{|\vec{R}-\vec{r}|}.$$

The functions $A_L(x)$ and $H_L(x)$ are equal to the modified spherical Bessel functions $i^L j_L(ix)$ and $i^{L+1}h_L^+(ix)$, respectively [46]. The notation $r_{<(>)}$ means the smaller (larger) of the values of r and R.

The projectile-electron potential (equation (10)) is represented here by

$$V_{pe}(\vec{R}-\vec{r}) = -\frac{Z_p - n_p}{|\vec{R}-\vec{r}|} + n_p \sum_{n=1}^{n_{max}} (A_n + B_n|\vec{R}-\vec{r}|)\frac{\exp(-\lambda_n|\vec{R}-\vec{r}|)}{|\vec{R}-\vec{r}|}, \tag{29}$$

where n_p is the number of bound electrons and the coefficients A_n, B_n and λ_n are obtained by fitting to the numerically determined potential from equation (10). The number of Bohr-like screened potential terms, n_{max}, corresponds to the number of electronic shells of each target atom. In this way, the function $f_L(r,R)$ used in equation (26) is obtained straightforwardly.

With the matrix elements from equation (24) the coupled-channel equations are solved numerically in order to obtain the coefficients a_i after the collision ($t \longrightarrow \infty$). For instance, the probability of ionizing the target from the ground state to a continuum state of energy ε, angular momentum l and projection m in a collision with impact parameter b is given by

$$\frac{dP_{l,m}}{d\varepsilon}(b) = \lim_{t\to\infty} |a_{\varepsilon,l,m}(b,t)|^2 \tag{30}$$

and to a empty bound state n

$$P_{n,l,m}(b) = \lim_{t\to\infty} |a_{n,l,m}(b,t)|^2. \tag{31}$$

The accuracy of the present computer code when restricted to perturbation theory (SCA mode) was checked against PWBA [1,47] and SCA [29,33] results for ionization and excitation. From the comparison a relative uncertainty of less than 0.1% for probabilities and about 2% for cross sections was inferred for different final states. It is noted that the uncertainty

in the cross section calculations is mainly due to the small number of impact parameter steps and continuum energies considered in this work. The numerical transition matrix elements agree to within 10^{-4} or better with analytical solutions for transitions between the lowest bound states. Finally, the accuracy of the coupled-channel code was checked against results of the well-established two-center code (AO +) by Fritsch [48,49]. When restricted to the same 20 target-centered bound states the results of both codes agree to within two to three digits for excitation probabilities ranging from 10^{-6} to 0.15. With the present code unitarity can be preserved to within about 10^{-7} if the damping factor F in equation (21) is set to unity.

The results coming from the coupled-channel method results agree with the predictions of the first-order perturbation theory (SCA) in the case of a small perturbation. Small perturbations correspond to either fast projectiles, large impact parameters or small projectile charges. Thus, the advantages of coupled channel calculations compared to first-order theories should show up especially at intermediate incident energies and for small impact parameters. In contrast to other coupled-channel calculations we do not use pseudostates to represent the electron continuum wave functions. Instead we use a large number of continuum wave-packets that are composed of a superposition of exact continuum eigenstates (up to 500 gerade states with partial waves up to $l = 10$), since the computation of the stopping power demands high accuracy of the emitted electron energy spectrum.

2.5. Ionization/stopping/straggling cross sections

2.5.1. Electronic

Each excited or continuum state corresponds to a well-defined energy transfer ΔE_i ($= E_i - E_0$). Then the cross section for such an energy-transfer process will read

$$\sigma_i = 2\pi \int_0^\infty b \, \mathrm{d}b P_i(b) \tag{32}$$

and average electronic energy loss $\bar{Q}(b)$ is given by

$$\bar{Q}(b) = \sum_i P_i(b) \Delta E_i \tag{33}$$

with the ionization and excitation probabilities P_i from equations (30) and (31). The electronic stopping cross section S_e and energy straggling W per atom can be computed directly from:

$$S_e = \sum_i \sigma_i \Delta E_i = 2\pi \int_0^\infty b \, \mathrm{d}b \, \bar{Q}(b) \tag{34}$$

and

$$W = \sum_i \sigma_i \Delta E_i^2. \tag{35}$$

It is noted that the above sums have to be replaced by integrals in the case of continuum states.

Figure 2 shows the comparison of the present coupled-channel results (solid curve) with other calculations for the total ionization cross section as well as for the electronic stopping power S_e of antiprotons on H. The dashed curve also represents coupled-channel calculations [50] using a large number of pseudostates. Both coupled-channel calculations provide similar results and are in rather good agreement with recent measurements [51] (symbols). Also displayed are results of first-order Born (PWBA) and the CDW-EIS model. As it can be seen from this figure, higher order effects become very important at low projectile energies. The PWBA calculations yield too large values of the electronic energy loss, since for antiprotons the polarization effect leads to a reduced electronic density along the ion path. In the CDW-EIS model [5] (dotted line) the initial and final states partially include the effect of the projectile potential (approximate two-center initial and final

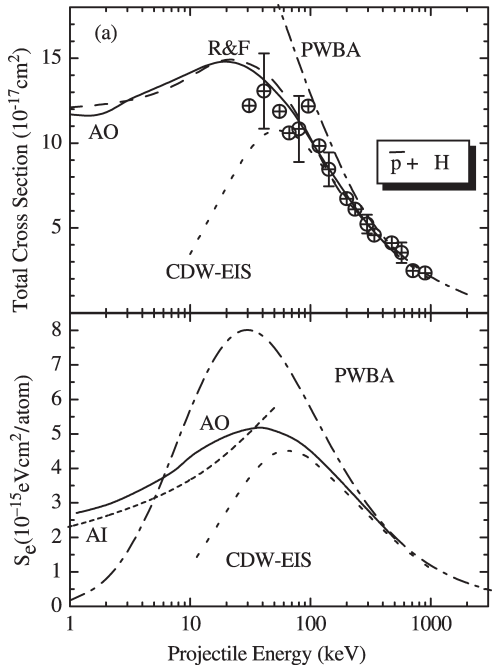

Fig. 2. Total ionization cross section and stopping power for antiprotons on hydrogen atoms.

states) and as a consequence the results at intermediate to high energies are significantly improved. However, a breakdown of this model is observed for energies below 70 keV. This is attributed to the incomplete treatment of the two-center effects and to the neglect of higher order residual projectile–target interactions in the CDW-EIS model. Furthermore, at low energies it is not able to describe the Fermi–Teller effect responsible for the slow decrease of the stopping power as a function of the projectile energy. The curve denoted by AI provides a simple model for this adiabatic ionization [52]. In this model the adiabatic potential curves for the electronic states in the field of the quasidipole formed by p and $\bar{p}$ are taken into account and a good agreement with AO results is observed for low energies.

2.5.2. *Nuclear*

The nuclear energy loss and the corresponding stopping cross section can also be calculated from the solution of classical equations for the projectile path. In equation (7) the interaction of the electron cloud with the residual target core was neglected. Thus, the projectile scattering angle θ is a more accurate quantity than the recoil energy in this model. Consequently, we search for a connection between the Q value, the projectile scattering angle, and the projectile energy loss. Considering conservation of energy and momentum, the kinetic energy transfer to the target atom is given by

$$T[Q] = \frac{4m_p m_t}{(m_p + m_t)^2} E\left(f \sin^2(\theta_{cm}/2) + \frac{1}{4}(1-f)^2\right) \tag{36}$$

with $f \equiv \sqrt{1 - Q/E(m_p + m_t)/m_t}$, E the ion initial energy, and θ_{cm} the projectile scattering angle in the center-of-mass system

$$\left(\tan\theta = \frac{\sin\theta_{cm}}{\cos\theta_{cm} + m_p/m_t}\right).$$

The nuclear stopping power per atom S_n may be computed directly from the impact-parameter integration of the nuclear energy loss.

At low incident energies the nuclear stopping process determines the slowing down of ions in the matter. Calculation with parameterized time-independent potentials have yielded stopping powers and ranges in good agreement with experimental data [53] except for some special systems [54]. These potentials correspond to static (frozen) electronic charge distributions. However, investigations of highly charged ions or negative particles require the treatment of collisional excitation processes and of the resulting dynamic target polarization. Any polarization during the collision will influence the projectile/target interaction potential. Hence, the nuclear stopping power is changed. It should be emphasized that the nuclear stopping may also be influenced by the electronic energy loss in a different fashion for

many-electron systems due to the formation of quasi-molecular orbitals that influence the excited potential [54].

We have used our atomic-orbital coupled-channel code to calculate dynamic curved projectile trajectories for protons and antiprotons in the field of polarized hydrogen atoms. According to Section 2.1, the electronic motion is treated quantum mechanically resulting in a time-dependent electronic density. The nuclear motion is determined simultaneously by Newtow's classical equation of motion and the nuclear energy transfer may directly be extracted. Figure 3 shows scaled nuclear energy loss cross sections for different incident light particles on atomic hydrogen. For fast projectiles the nuclear energy loss cross section S_n behaves roughly as $\ln(E_p)/E_p$ and a maximum of S_n is found at about 50 eV. Thus, $S_n E_p/\ln(E_p/10\ \text{eV})$ is nearly constant when E_p is varied from 1 to 300 keV. The lowest curve in Fig. 3 is the well-known ZBL stopping-power prediction [53]. It relies on an approximate

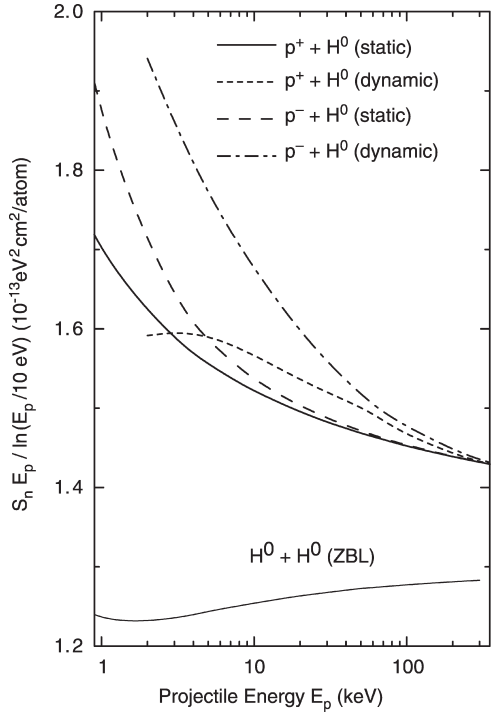

Fig. 3. Scaled nuclear stopping power as a function of the projectile energy for protons (short-dashed and thick solid line), antiprotons (long-dashed and dash-dotted lines) and neutral hydrogen incident on hydrogen atoms. Thin solid line: ZBL prediction [53] for neutral projectiles. For two of the curves (short and long-dashed) dynamic target polarization has been accounted for in the calculation.

treatment of the static interaction between a projectile and the target atom. Since both collision partners are screened in this case the results are lower than the static results for incident protons and antiprotons. For antiprotons at low velocities the static results are slightly larger than for protons because the distance of closest approach r_0 is smaller for antiprotons.

Especially at low energies, the results of dynamic calculations show a significant deviation from the static ones. At 2 keV the antiproton results with polarization lie about 20% above the static results. Furthermore, S_n clearly shows a different energy dependence for antiprotons and protons. The reason for this deviation is depicted in Fig. 4. At large impact parameters negative projectiles repel the target electron cloud and positively charged particles attract the electrons. Hence, in both cases the projectile is deflected towards to the target atom and the deflection is larger than in the static case. The situation is different for the positive ions at small impact parameters; at larger internuclear distances the projectile is attracted by the electron cloud, but at small distances the Coulomb force between the nuclei leads to a sudden projectile deflection away from the target nucleus. At low energies, this repulsion is even enhanced due to a reduction of r_0. At intermediate impact parameters, the attraction and the repulsion are of the same strength

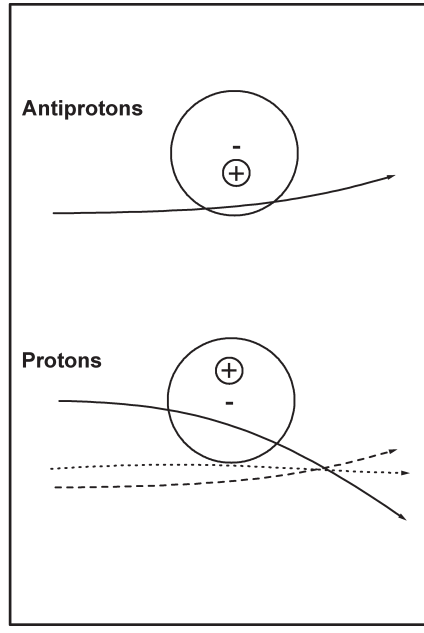

Fig. 4. Scheme showing typical projectile trajectories of protons and antiprotons in the field of polarized target atoms.

and the trajectory is nearly a straight-line. Thus, the nuclear energy transfer is strongly reduced and at a certain impact parameter it is even zero.

Finally, at low incident energies, larger impact parameters gain importance and the dynamic results exceed the static ones. On the contrary, for fast positively charged projectiles the zero-crossing of the projectile scattering angle (at impact parameters of about 2 a.u. in the case of H) leads to slightly reduced dynamic nuclear stopping cross sections.

2.6. Two-center calculations

The procedure outlined in the previous sections to solve the time-dependent Schrödinger equation should be highly accurate as long as electron capture is of minor importance. An exact description of an even single projectile-centered state would require an infinite number of target-centered states in the basis set. The use of huge basis sets of target-centered states can in fact describe, in same cases [12], the energy loss due to the capture process but in general full two-center calculations have to be performed.

The present coupled-channel calculations also allow for the inclusion of projectile-centered states according to following expansion

$$\Psi_e(t) = \sum_n a_n(t)\phi_n(\vec{r},t), \tag{37}$$

where the wave functions $\phi_n(\vec{r},t)$ are either time-dependent target-centered states (bound or wave packet continuum states) or projectile-centered states. The coupled-channel equations are obtained from the more general matrix elements for transitions between two moving reference frames

$$\langle\phi_m(\vec{r},t)|\mathcal{H}_e - i\frac{\partial}{\partial t}|\Psi_e(t)\rangle \tag{38}$$

and they read

$$\sum_n \langle\phi_m(\vec{r},t)|\phi_n(\vec{r},t)\rangle i\frac{da_n}{dt} = \sum_n a_n(t)\langle\phi_m(\vec{r},t)|\mathcal{H}_e - i\frac{\partial}{\partial t}|\phi_n(\vec{r},t)\rangle. \tag{39}$$

The matrix elements can be calculated as

$$\begin{aligned}&\langle\phi_m(\vec{r},t)|\mathcal{H}_e - i\frac{\partial}{\partial t}\left|\phi_n^P(\vec{r},t)\right\rangle \\ &\quad= \langle\phi_m(\vec{r},t)|V_t + \mathcal{H}_p - i\frac{\partial}{\partial t}|\phi_n^p(\vec{r},t)\rangle \\ &\quad= \langle\phi_m(\vec{r},t)|V_t|\phi_n^p(\vec{r},t)\rangle\end{aligned} \tag{40}$$

and

$$\begin{aligned}&\langle\phi_m(\vec{r},t)|\mathcal{H}_{\rm e}-{\rm i}\frac{\partial}{\partial t}|\phi_n^t(\vec{r},t)\rangle\\&\quad=\langle\phi_m(\vec{r},t)|V_{\rm p}+\mathcal{H}_{\rm t}-{\rm i}\frac{\partial}{\partial t}|\phi_n^t(\vec{r},t)\rangle\\&\quad=\langle\phi_m(\vec{r},t)|V_{\rm p}|\phi_n^t(\vec{r},t)\rangle,\end{aligned}$$

for exact time-dependent target-centered states $\phi_n^t(\vec{r},t)$ or projectile-centered $\phi_n^{\rm p}(\vec{r},t)$ states.

Since the wavepackets $\phi_n^t(\vec{r},t)={\rm e}^{-{\rm i}\bar{E}t}(\Delta E)^{-1/2}\int_{\varphi_{\rm E}}(\vec{r},t)\,{\rm d}E$ are not exact solutions of the time-dependent Schrödinger equation for the target atom, there is an extra term

$$\begin{aligned}&\langle\phi_m(\vec{r},t)|\mathcal{H}_{\rm e}-{\rm i}\frac{\partial}{\partial t}|\phi_n^t(\vec{r},t)\rangle\\&\quad=\langle\phi_m(\vec{r},t)|V_{\rm p}|\phi_n^t(\vec{r},t)\rangle+\langle\phi_m(\vec{r},t)|^{-{\rm i}\bar{\varepsilon}t}(\Delta E)^{-1/2}\int(\varepsilon-\bar{\varepsilon})|\varphi_\varepsilon(\vec{r},t)\rangle{\rm d}\varepsilon,\end{aligned}$$

which is not zero in the case of capture matrix element ($\langle$projectile$|\cdots|$target$\rangle$). It is noted that this term does not appear in the case of target–target matrix elements. All matrix elements are calculated numerically for hydrogen-like projectile wave-functions.

The capture probabilities are then obtained from the coefficients a_n from the expansion (37). For the capture energy-loss, the translation factor energy $v^2/2$ has to be added to the transition energy between the target and projectile states. In conclusion, the treatment of electron capture requires to account for phase factors of the moving reference systems, for non-orthogonal states at both centers and to consider the time dependence of wave packets. Such calculations are, therefore, much more time consuming than target-centered computations.

3. HIGHER ORDER EFFECTS

The coupled-channel calculations allow for accurate calculations of higher order effects. At high energies the electronic energy loss may be expanded in terms of the projectile charge $Z_{\rm p}$ according to

$$Q(b)=q_1Z_{\rm p}^2+q_2Z_{\rm p}^3+q_3Z_{\rm p}^4+\cdots \tag{41}$$

The quadratic term is the leading one at high energies. It is well described by first-order Born theory and involves only direct ionization and excitation of the target atom. With decreasing ion energy higher order effects become important. They either depend on the sign of the projectile charge $Z_{\rm p}$

(polarization and binding effects) or only on the absolute value of Z_p (Magnus [55] and Bloch [19] corrections). All higher order effects (deviations from the Z_p^2 proportionality) can be related to multiple successive interactions of the active electron with the projectile and the (screened) target within a single collision. The number of these interactions increases for high projectile charges, small impact parameters and low projectile velocities. We can distinguish different higher order contributions as a function of the strength of the perturbation.

For small perturbations of outer-shell electrons the polarization of the electronic density appears first. Positively charged particles attract and negatively charged projectiles repel the electron cloud during an early stage of the collision, which leads to a change in the density around the projectile path and correspondingly to a change in the stopping power. This is a second-order effect (proportional to Z_p^3).

By decreasing the ion energy the influence of the projectile is no longer a small perturbation and effects such as saturation and binding-energy modifications will appear. In standard first-order treatments, the sum over all probabilities exceeds one since no reduction of the initial-state population is accounted for. This leads to an artificial creation of electrons (overestimated stopping power proportional to Z_p^4). The corresponding experimentally observed saturation (stopping power reduction compared to Z_p^2 for heavy ions) may roughly be described within the unitary first-order Magnus approximation [55]. A different treatment by Bloch [19] also takes into account this effect and the term proportional to Z_p^4 agrees quite well with the one from coupled-channel calculations.

For inner-shell electrons the so-called binding effect gains importance. The resulting change of the stopping power is proportional to Z_p^3 but its sign is opposite to the change induced by the polarization effect. The binding effect can be viewed as an increased binding energy of the bound electron in the vicinity of positively charged projectiles, which reduces the stopping power. It is a second-order effect (proportional to Z_p^3) that may be included in a perturbative treatment by consistently accounting for the diagonal matrix elements of the projectile/electron interaction or by including the mean binding effect in a perturbed stationary-state model [56].

Finally, at low energies the projectile represents a strong perturbation and effects such as electron capture for positive projectiles and adiabatic ionization (Fermi–Teller effect [52]) for negatively charged projectiles turn out to be very important. The electron capture may be viewed as a very strong polarization effect (target electrons are attracted by and finally travel with the projectile). If the electronic motion is described in a target-centered basis all orders of the perturbation are necessary to yield the time-dependent electron-density. In other words, the interaction between electron and projectile never stops. In the Fermi–Teller effect, collisions with negative heavy projectiles are involved. For the case of antiprotons on H, the electrons

move in the field of a transient 'quasidipole' formed by the heavy particles. The electronic states of the quasidipole experience a rapid loss of binding energy when the distance between the heavy particles decreases, and become even unbound at a certain non-zero 'critical' distance.

Besides these effects we also observe for increasing perturbations (high Z_p at low energies) a diffusion like effect in the energy spectrum of emitted electrons [7]. The first excitation step gives rise to an excitation spectrum with a maximum at low energy transfers. Successive interactions (continuum–continuum couplings) yield a broadening of the excitation spectrum. Hence, low electron energies are suppressed due to this diffusion-like process and the mean stopping power as well as the straggling are enhanced. This energy-diffusion effect may be viewed as the onset of the Fermi-shuttle effect, where multiple head-on collisions between projectile and electron in the field of target lead to extremely high electron energies.

Figure 5 shows a contour plot of the time-dependent electron density for a hydrogen atom disturbed by a positively (displayed on left) and negatively (displayed on right) charged particle at 10 keV with an impact parameter of 1 a.u. These electronic densities correspond to a cut in the collision plane and were obtained directly from the calculated transition amplitudes $a_i(t)$ according to

$$\rho(\vec{r},t) = \sum_{i,j} a_i a_j^* \, \mathrm{e}^{-\mathrm{i}(E_i - E_j)t} \varphi_i(\vec{r}) \varphi_j^*(\vec{r}) \tag{42}$$

using about 200 gerade states. An inspection of this figure shows several interesting features. First, the positively charged particle (proton) attracts the electron on the incoming path; the so-called polarization process. One may see that the electron density moves towards the projectile. The opposite effect takes place for the negatively charged particle (antiproton).

Second, for protons at the distance of closest approach, the maximum of the electron-density points to the backward direction at an angle of about 120° with respect to the beam axis. It is clearly visible that the electron density lies behind the projectile, although the proton is attracting the electron. The reason for this behavior is a delayed response of the electron cloud (the inertia due to the electron mass). Third, the proton enables electron-capture in the outgoing path of the collision and large fraction of the electron density is finally bound to and moving with the projectile. Since an antiproton repels the target-electron, the electron density near the projectile on the outgoing path of the collision is almost zero.

For collisions of antiprotons with atomic hydrogen, a quasidipole is formed during the collisions. The dipolar antiproton–proton system does not support bound states for inter-particle distances below 0.64 a.u. [52]. For finite velocities and larger impact parameters b (in the figure, $b = 1$) there is still a significant ionization contribution. As can be observed in the figure at

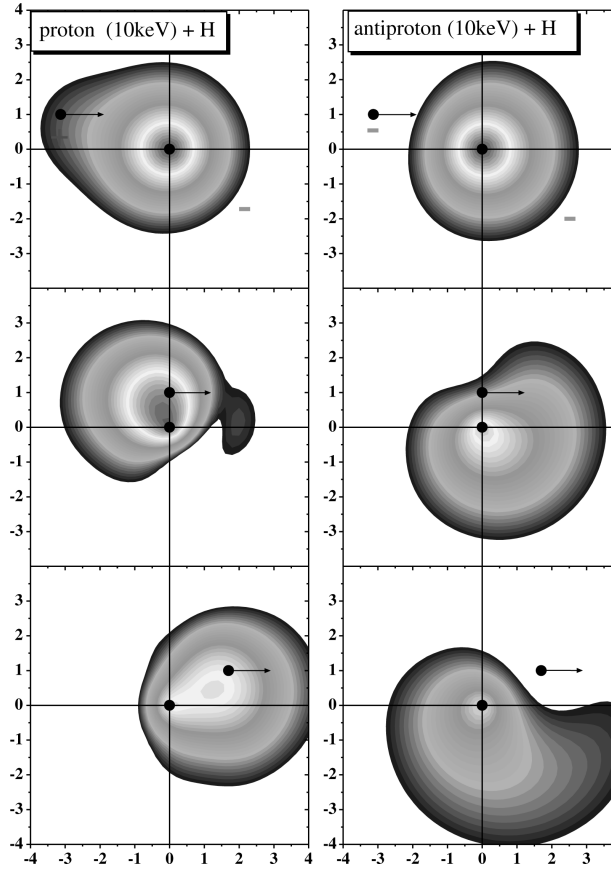

Fig. 5. Contour plot of the time-dependent electronic density of a hydrogen atom disturbed by a 10 keV proton (on left) and antiproton (on right) at $b = 1$. The plot corresponds to a cut of the density across the collision plane.

the distance of closest approach there is a high transition probability (blowing up of the density).

The electronic energy loss for proton, antiproton, helium and antihelium on H at 500 keV normalized to first-order Born (SCA) results is shown in Fig. 6 as a function of the impact parameter. Results for particles are represented by solid lines and for antiparticles by dashed lines. Deviations from the horizontal line (ratio equal to one) correspond to higher order effects. A fictitious projectile charge $Z_p = \pm 0.5$ is also displayed in order to observe the tendency of the energy loss as a function of the projectile charge. For large impact parameters the difference between the energy loss for particles and antiparticles is due to the polarization effect. The energy loss

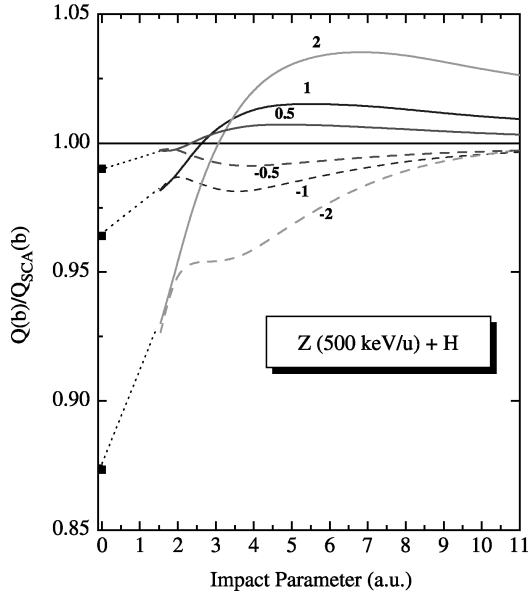

Fig. 6. The electronic energy loss normalized to first-order Born results for bare projectiles with $Z_p = \pm 0.5, \pm 1$ and ± 2 at 500 keV/u on hydrogen. Results for positively charged particles are represented by solid lines and for negatively charged ones by dashed-lines. The squares at $b = 0$ represent a calculation with improved accuracy. The dotted lines show the transition between the two AO calculations.

for positively charged particles is larger than for negatively charged particles and the difference is nearly symmetrical for low Z_p.

For small impact parameters one may see an overall reduction of the energy loss as a function of $|Z_p|$. This corresponds to Z_p^4 effects overshadowing the Z_p^3 ones (polarization and binding effects). The binding effect can enhance or reduce the probability to excite or ionize the target atom. It always leads to a significant reduction of the polarization effect at small impact parameters. It should be noted that although the overall numerical uncertainties are about 2%, they can be much larger for impact parameters smaller than 2 a.u. For central collisions ($b \rightarrow 0$), we can, however, strongly increase the size of the basis set by using only states with angular momentum projection m equal to zero due to the azimuthal symmetry of the time-dependent electronic wave function. Calculations performed with almost 150 of these states show that the Barkas effect, the difference between the energy loss for positively and negatively charged particles, is nearly zero (to within the numerical uncertainties) for unscreened projectiles. This result seems to be independent of the target potential since it is also observed for a harmonic-oscillator target [57].

4. PHOTON VS. CHARGED-PARTICLE IONIZATION

Here we apply the coupled-channel method to calculate photo ionization of atomic hydrogen by short (femtosecond) laser pulses at high power densities (up to 5×10^{14} W/cm^2). A classical electro-dynamical field approximates the laser/atom interaction, according to (in the Coulomb gauge)

$$V_{\text{laser}}(t) = -\vec{r}\cdot\vec{E}(t) \tag{43}$$

with

$$E(t) = E_0 \exp\left(-\frac{t^2 4 \ln 2}{\Delta t^2}\right)\cos(\omega t). \tag{44}$$

The time dependent shape of this field is given by a cos-function with amplitude E_0 enveloped by a Gaussian centered at the time $t = 0$ with full width at half maximum (FWHM) Δt representing the laser pulse length.

The transition matrix elements are non-vanishing if the dipole selection rules are fulfilled. The dipole approximation is valid, since the wavelength of the laser is large in comparison to the atomic radius. For a linear polarized laser beam, with the electrical field in the z-direction, this means $\Delta l = \pm 1$ and $\Delta m = 0$. The coupled-channel method is used to determine the coefficients of the wave function by solving the system of coupled-channel equation (3) for 764 eigenstates of the target. These consist of 45 bound states up to $n = 9$ and wave packets up to continuum energies of 18 eV and $l = 9$, all coupled by the corresponding dipole matrix elements for linearly polarized light. Although we have performed large-scale computations, there will be an upper limit for the laser-pulse width Δt_{p}, since the corresponding energy broadening ΔE_{p} should exceed the energy difference of neighboring continuum states. Furthermore, there will be a maximum possible power density I related to the upper limit of electron energies and partial waves l in the calculation. These two computational limits have been explored here.

As a result of the calculations we obtain the differential probability dP of ionizing an atom in an energy interval dε depending on the electron energy. Figure 7 represents such an ionization probability calculated for hydrogen atoms excited with a wavelength of 260 nm and a pulse duration of 10 fs. The probability is enhanced at integer multiples of the photon energy ($nh\nu$ where the minimum number n is given by the multiple at which the ionization limit is exceeded (in case of hydrogen $n = 3$). Sometimes a small shift of the harmonics is observed which is caused by second-order terms in the perturbation theory like Stark effect and ponderomotive force [58]. The differential probability is increased with a high power of the laser intensity. This is seen in the broadening and increase of the ionization peak structures with increasing laser intensity in Fig. 7. The broadening results from

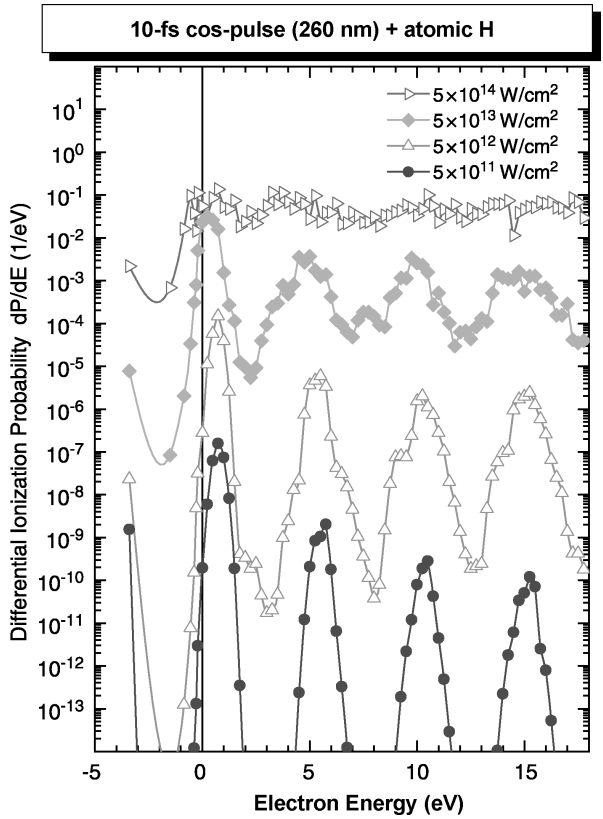

Fig. 7. Differential ionization probability of hydrogen at 260 nm calculated for four laser intensities.

a reduced effective interaction time, since the ground state may be depopulated on a sub-femto second time scale for high laser intensities.

Resonant and also non-resonant multiphoton transitions are well reproduced with the program. This was tested by changing the wavelength from 200 to 260 nm.

Figure 8 displays the corresponding 3-photon ionization cross sections $\sigma^{(3)}/I^2$ in comparison with literature values [59]. The corresponding N-photon cross sections in units of $\mathrm{cm}^{2N}/\mathrm{W}^{N-1}$ are defined as

$$\sigma^{(N)}/I^{N-1} = P/F/I^{N-1}/\tau_{\mathrm{eff}}(N), \tag{45}$$

where P is the ionization probability, F is the flux in photons/cm^2/s and I is the power density in W/cm^2. The effective interaction time $\tau_{\mathrm{eff}}(N)$ is equal to the width of the light-pulse Δt_{p} divided by $1.33N^{0.5}$ for a long Gauss packet.

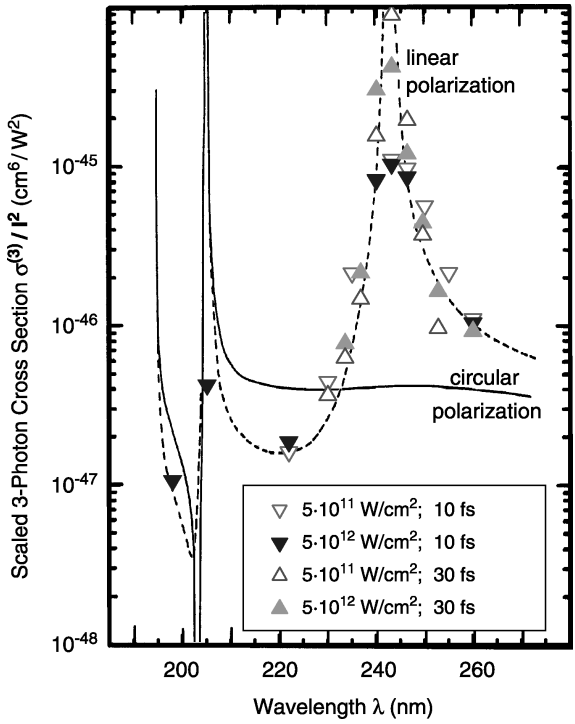

Fig. 8. Scaled 3-photon ionization cross sections $\sigma^{(3)}/I^2$ as a function of the wavelength λ for two power densities I and two-pulse lengths Δt_p. Standard results for asymptotically long times and asymptotically low power densities are taken from Ref. [59] and shown as dashed (linear polarization) and solid (circular polarization) curves.

For light with linear polarization 3 overlapping Fano-peak profiles are visible in Fig. 8. These peaks correspond to resonance ionization with the intermediate bound states 2s (at 243 nm), 3s/3d (at 205 nm) and 4s/4d (at 195 nm). It is seen that our coupled-channel results (symbols) are in good agreement with the results of third-order perturbation theory [59]. We predict a broadening of the 2s-resonance maximum due to the short pulse durations of only 10 and 30 fs. For the 30 fs-pulses there is a clear indication for non-perturbative effects as the cross section for $I = 5 \times 10^{12}$ W/cm^2 is suppressed (due to induced photon emission) in comparison with the one for 5×10^{11} W/cm^2 at the center of the peak. For a wavelength of 253 nm at the lower power density we find a significant deviation between our results and the reference curve. This deviation is most likely due to the finite numerical energy steps of 0.25 eV that exceed the photo-ionization peak-width of 0.17 eV for this case.

Figure 9 displays the integrated ionization probability of H after pulsed optical excitation as a function of the maximum cycle-averaged laser-power density. Calculations have been performed for wavelengths between 80 and 590 nm and for pulse lengths between 10 and 30 fs (Fig. 8). All results (symbols and fitted thin curves) show a monotonous increase as a function of the power density I and nearly 100% ionization is reached for $I = 5 \times 10^{14}$ W/cm^2. At low power densities the curves are proportional to I^N, in agreement with perturbation theory.

The following restrictions have been found to the application of coupled-channel calculations for the computation of pulsed-laser ionization. The dipole approximation restricts the photon energy to <1 keV in the current treatment. This, however, does not pose a strict condition since a partial-wave expansion of the laser field may be used, similar to as in the case of screened Coulomb potentials. In comparison to ion/atom collisions, typical photon/atom interaction times are extremely long. An upper limit of the pulse width $\Delta t_p = 100$ fs at intermediate laser-power densities follows from the numerically restricted density of continuum states.

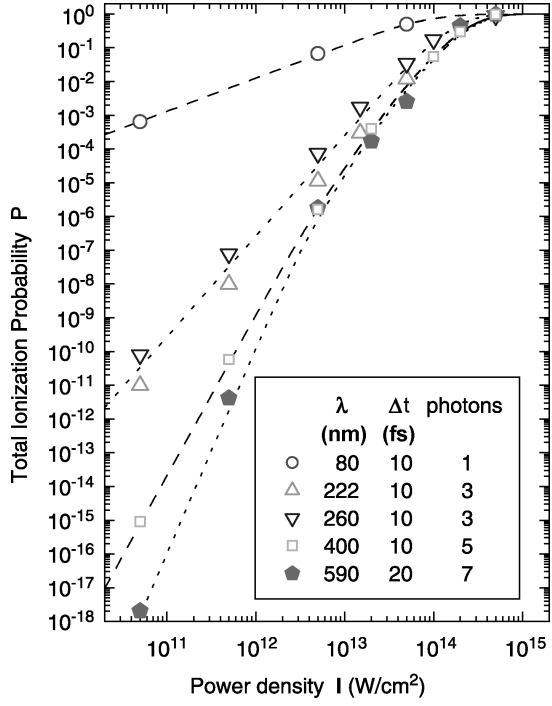

Fig. 9. Total ionization probability of H as function of the power density I for different non-resonant laser wave lengths and pulse widths.

High power densities ($\gg 10^{14}$ W/cm^2) and small laser frequencies ($\lambda > 600$ nm) are related to extremely high orders of perturbation theory. This requires basis sets extending to high values of ($l \gg 15$) and high ejected-electron energies ($\varepsilon \gg 20$ eV). With the help pf P/Q space methods [60] the range of validity of coupled-channel calculations may be extended in this case.

5. COMPARISON WITH MEASUREMENTS

The first coupled-channel calculations for total and differential energy losses were performed for very simple systems such as H on H, He [11,12,61]. Later theses calculations have been extended to more complex systems such as the inner-shells of Al and Si [22,24]. Good agreement with experimental data has been found and the remaining discrepancies have been attributed to multielectron processes.

5.1. Gas targets

5.1.1. Angular dependence

A direct measurement of the electronic energy loss as a function of the impact parameter is a hard task to be performed from the experimental point of view and only a few experiments have been performed for fast light ions. Experiments in gas targets under single collision condition provide a more direct and precise comparison of the theoretical results with the experimental data. Here we compare the results of the coupled-channel method for collisions of protons with He as a function of the projectile scattering angle.

Winter and Auth [61,62] have directly measured the energy loss of protons impinging on gas targets as a function of the final projectile scattering angle. For helium targets they have observed a peak structure (with a width of about 0.6 mrad) in the mean energy loss at scattering angles around 0.5 mrad. The angular dependence of the energy loss for 200 keV is shown in Fig. 10. The peak can be related to the so-called binary process: if the projectile interacts with a free electron initially at rest, each final electron energy corresponds to a well-defined impact parameter and projectile scattering angle. Small but non-zero impact-parameter collisions between proton and electron give rise to a maximum projectile-scattering angle of 0.5 mrad for this case. The angle is given by the mass ratio of an electron and the projectile.

The scattering of a proton with a He atom is at least a three-body problem involving the projectile–active-electron and the projectile–target-core interaction (the four-body problem is reduced to a three-body problem by application of the independent-electron frozen-core model). Therefore, the conversion from impact parameter to projectile-scattering angle should be done carefully. For incident energies above a few hundred eV/amu and for

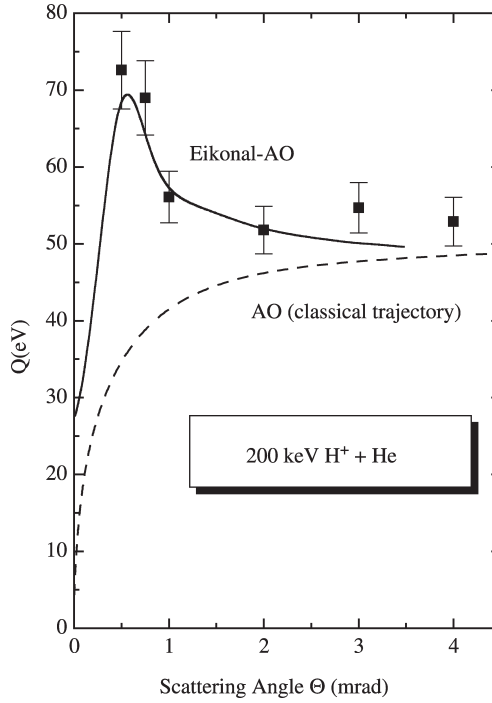

Fig. 10. Mean electronic energy loss for H^+ incident on He at 200 keV as a function of the projectile scattering angle. Closed squares with error bars : experimental results from Ref. [61]. Solid line: (three-body) Eikonal-AO results; dashed-line: (two-body) AO results for mean-field projectile trajectories.

small projectile scattering angles, this transformation can be performed employing the Eikonal method [34]. Basically, the transition amplitude as a function of projectile scattering angle is obtained from the impact parameter dependent amplitudes $a_i(b)$ by a Hankel transformation. The two-electron amplitude can then be obtained from the product of two single-electron amplitudes. The differential scattering amplitude for a small projectile scattering-angle Θ, in the Eikonal approximation [34], reads

$$f_{n_1,l_1,m_1;n_2,l_2,m_2}(\Theta) = i^{m_1+m_2} K \int_0^\infty b\,\mathrm{d}b J_{|m_1+m_2|}(K\Theta b) \times \left(a_{n_1,l_1,m_1}(\infty,b) a_{n_2,l_2,m_2}(\infty,b) \exp\left(-\mathrm{i} \int \mathrm{d}t \frac{Z_\mathrm{p} Z_\mathrm{t}}{R} \right) - \delta_{1,2;\mathrm{GS}} \right)$$

for a bare projectile with charge Z_p and for a target nuclear-charge Z_t. The principal quantum number is denoted n_i and l_i, m_i are quantum numbers associated with the angular momentum and angular momentum projection of

the ith electron. $\delta_{1,2;GS}$ is equal to one only when both electrons are in the ground state, otherwise it is zero and $J_m(z)$ are Bessel functions of integer order. K is the momentum of the projectile in the laboratory frame. The above transformation accounts for the combined influence of the target nuclear potential and individual electronic transitions on the projectile motion. Then, the mean electronic energy-transfer can be directly computed from

$$Q(\Theta) = \frac{\sum_i |f_i(\Theta)|^2 \Delta E_i}{\sum_i |f_i(\Theta)|^2} \tag{46}$$

since each two-electron state i (specified by $n_1, l_1, m_1; n_2, l_2, m_2$) corresponds to a well-defined energy transfer $\Delta E_i = E_i - E_0$ (E_0 is the initial state energy).

Figure 10 displays the results of our mean energy loss calculations for protons incident on helium at 200 keV as a function of the projectile scattering angle by using the Eikonal transformation (solid line) in comparison with the experimental data of Winter and Auth (closed squares). The dashed lines represent results that are also based on AO calculations but the conversion to projectile-scattering angle was performed by solving the classical Hamilton equations for an averaged heavy-particle Hamiltonian (see equation (7)) that is computed from the time-dependent electron density. This mean-field trajectory treatment goes beyond models that use predetermined straight-line or hyperbolic trajectories. In fact, the averaged potential used in the definition of the average trajectory is unable to account for the kinematics of a violently ionizing collision in contrast with the eikonal method. These violent collisions enhance the mean energy transfer by a factor of about two for this case. Deviations between mean-field and Eikonal-AO results extend up to $\Theta \approx 3$ mrad and point to the importance of three-body effects. Further details may be found in Ref. [61].

5.1.2. *Stopping cross section*

Figure 11 shows our coupled-channel (atomic orbital) results for the electronic stopping cross sections corresponding to hydrogen beams penetrating He gas. In order to calculate the equilibrium mean stopping power we must consider the charge state distribution of the projectile and the fact that we are restricted to only one active electron. Then, we have to calculate the energy loss in three reaction classes:

(1) $H^+ + He^0 \rightarrow H^+ + He^*$ or (electron capture)
(2) $H^0 + He^0 \rightarrow H^0 + He^*$
(3) $He^0 + H^0 \rightarrow He^0 + H^*$

where $*$ includes excitation and ionization as well. For case 1 we have evaluated the electronic energy loss due to the electron capture process.

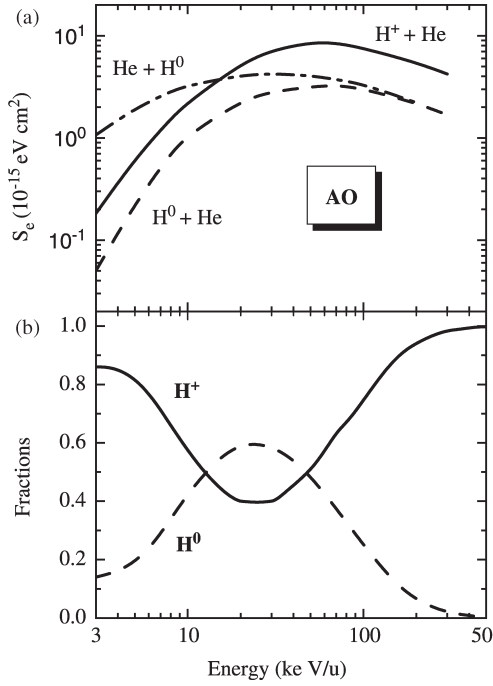

Fig. 11. (a) Coupled-channel results for electronic stopping cross section for H^+ and H^0 beams incident on He vs. incident energy (solid and dashed lines). Ionization and excitation of projectile, in the case of the H^0 charge-state fraction, is accounted for by considering the collision system $He + H^0$ (dot-dashed line). (b) Experimental equilibrium fractions for hydrogen beams in helium gas, from Ref. [63].

Ionization and excitation of the target electrons have been computed for 1 and 2. Case 3 provides the energy dissipation by projectile electron loss and projectile excitation. The energy loss involving neutral collision-partners ($H^0 + He$ and $He + H^0$) is basically due to target or projectile ionization. Excitation of the target or the projectile is of minor importance. The same holds true for collisions between H^+ and He at high energies ($E > 100$ keV). However, the main contribution at low projectile energies stems from the capture of target electrons into the projectile 1s state. From Fig. 11 we can see that the partial electronic stopping power for bare hydrogen is dominant at high energies whereas excitation and ionization of the projectile yield the highest partial cross section at low velocities. Nevertheless, the projectile ionization leads to an enhancement of the H^+ charge-state fraction at low velocities and consequently the contribution of H^0 to the stopping processes is reduced. The experimental equilibrium fraction [63] for hydrogen beams in He gas

are shown in Fig. 11. The H^+ fraction increases for high and low energies as well. The neutral fraction is only significant for intermediate ion velocities. This means that the $H^+ + He$ collisions dominate the low energy part of the stopping power. For energies around 30 keV/u, all reaction classes are equally important.

In Fig. 12 the equilibrium mean total stopping cross section per atom for $H + He$ collisions is presented in comparison with experimental data of different groups [64–69]. The solid curve represents the values of Fig. 11 weighted with the corresponding charge-state fractions (also displayed in Fig. 11, the contribution due to H^- can be neglected [63]). Special attention should be drawn to the low energy stopping power data which was recently measured by Golser and Semrad [69]. At energies below 10 keV experimental and theoretical results agree within 5% or better.

At 30 keV/u we find the largest deviation between the measured stopping power and our calculated values of about 12%. This may be attributed to an overestimation of cross sections for multielectron processes because of the use of the independent particle model. We emphasize that the present calculation does not properly take into account events in which more than one electron is actively involved, e.g., double target ionization or excitation and simultaneous projectile and target ionization.

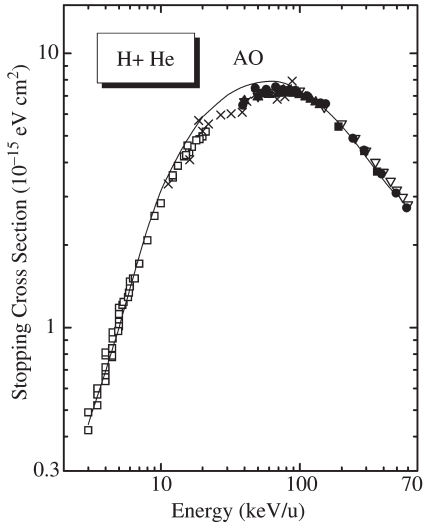

Fig. 12. Equilibrium mean stopping cross section per atom for hydrogen beams penetrating He gas. Present atomic orbital (AO) calculation (solid line). Experimental values: open triangles [64,65], closed squares [66], closed triangles [67], closed circles [68], open squares [69].

5.2. Solid targets

Here, we briefly describe a comparison with experimental channeling energy loss data for He ions in Si [22,23]. Coupled-channel calculations were performed for He^+ and He^{2+} on the Si inner shells. The energy-loss term associated with the Si-valence electrons was obtained from the experimental stopping cross section of Ref. [70] by subtracting the calculated contributions involving Si inner-shell and He electrons. The He charge-state distribution was taken from experimental results under channeling conditions from Ref. [71] (see insert in Fig 13) and the sum of the energy loss for each Si atom located across the channel was averaged according to the ion flux distribution [22]. Further details of the solid-state energy-loss treatment maybe found in Ref. [22].

Figure 13 shows the stopping power of He ions moving through the Si crystalin the $\langle 100 \rangle$ channeling direction. The symbols correspond to recent experimental data [22,72] for the channeled energy-loss and the solid line represents accurate experimental stopping values for a random direction [70]. Experiments at 800 keV with He^+ and He^{2+} ions show that charge equilibrium is reached at a depth of about 50 Å. We expect this distance to increase by an order of magnitude for 5 MeV He ions. Since the mean charge state of fast ions is close to two and the measurements above 1000 keV were performed with He^{2+} ions there should be no significant deviation from the assumed equilibrium charge-distribution.

The results of the AO calculations (dashed-line) for the projectile-energy dependence of the electronic stopping power under channeling conditions agree with the data to within the experimental uncertainty. For ion energies above 1.2 MeV (see insert in Fig. 13 for the He charge-state fractions), the He^{2+} fraction is dominant and the main physical process responsible for the reduction of the energy loss under channeling conditions compared to random directions is the suppressed inner-shell ionization (L-shell) of Si atoms.

The energy region from 1.2 up to 5 MeV is close to the maximum of the stopping cross section due to Si L-shell electrons and only non-perturbative calculations (including many higher order terms) are reliable in this energy region. By comparing the AO results with first-order ones at 2 MeV we obtain a difference of about 40% for $b = 1.3$ Å (middle of $\langle 100 \rangle$ channel). For energies below 1.2 MeV, the influence of charge-changing processes begins to be significant. The present energy-loss results as a function of the projectile energy are most sensitive to the computation of the inner-shell contribution at random directions, since under channeling conditions they are determined by the contribution of the valence excitations. The inner-shell contribution under channeling condition is suppressed by 75% at 5 MeV). Thus, a comparison with the angle dependent energy-loss data provides more information about the impact-parameter dependence of the energy loss [22].

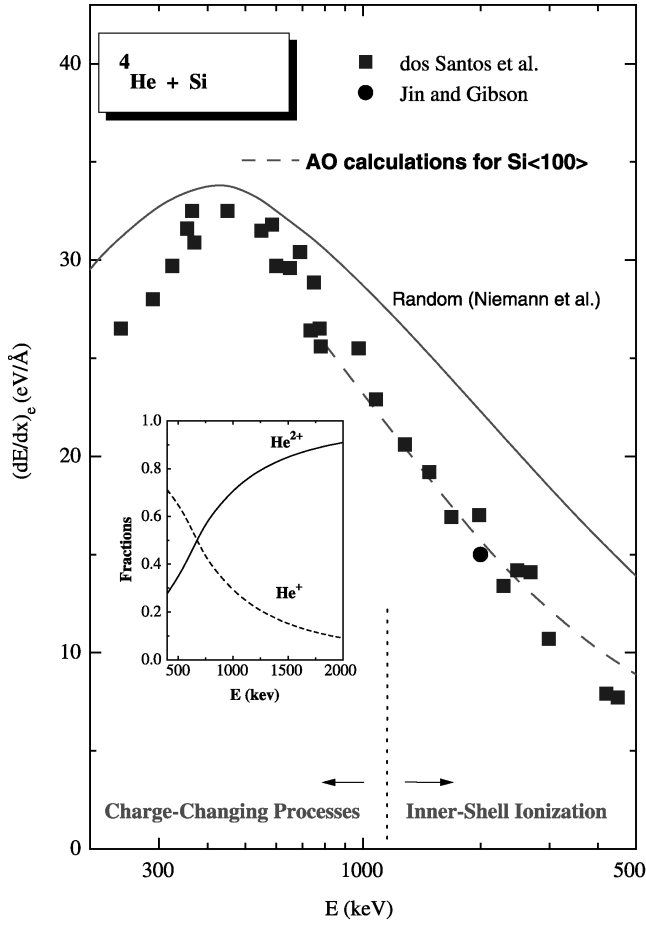

Fig. 13. Electronic stopping power as a function of the ^{4}He energy for the ⟨100⟩ Si direction.

6. SIMPLE MODELS FOR THE ENERGY LOSS

The coupled-channel calculations are used as benchmark results to check simple models of the impact parameter dependence of the electronic energy loss. A detailed description of such models (convolution approximation) may be found elsewhere [25,26]. Here we present only a short outline of the method. The electronic energy loss involves a sum over all final target states for each impact parameter. Usually this demands a computational effort that precludes its direct calculation in

a computer simulation code. Therefore, we search for an approximate solution without the necessity of performing a large-scale calculation.

In recent works [25] we have proposed a simple formula for $Q(b)$ (called PCA) that virtually reproduces SCA results for all impact parameters for bare and also for screened projectiles.

The following simple formula

$$Q(b) = \int \mathrm{d}^2 r_\mathrm{T} \mathcal{K}(\vec{b} - \vec{r}_\mathrm{T}) \int \mathrm{d}z \rho(\vec{r}_\mathrm{T}, z) \tag{47}$$

with

$$\mathcal{K}(b) = \frac{2Z^2}{v^2 b^2} h(2vb/\eta) \sum_i f_i g\left(\frac{\omega_i b}{v}\right) \tag{48}$$

joins smoothly all regions of impact parameters b for which two-body ion-electron (small b) and dipole (large b) approximations are valid. The function $h(2vb)$ [25] approaches zero for $b \ll 1/v$ (relative impact parameter smaller than the electron de Broglie wavelength in the projectile frame) and it reaches 1 for large values of b. The first two terms in equation (48) resemble the classical energy transfer to a statistical distribution of electrons at rest and describe violent binary collisions. The last term, involving the g function [25] and the oscillator strengths f_i, accounts for the long ranged dipole transitions. The first integral $\int \mathrm{d}^2 r_\mathrm{T} \cdots$ in equation (47) describes a convolution with the initial electron density also outside the projectile path and yields nonlocal contributions to the energy loss. It is noted that these nonlocal contributions are neglected in most previous simple energy loss models. With the parameter η equal to one, this formula mimics the first-order Born approximation very well [25]and it is denoted PCA (perturbative convolution approximation). For increasing projectile-charge first-order calculations (on which PCA is based) break down. They do not take in account, for instance, that each electronic transition gives rise to an increased final-state population and a corresponding reduction of the initial state population. It is clear that the ionization probability cannot increase indefinitely with the strength of the perturbation (the so-called saturation effect). Since these ionization processes come mostly from small impact parameters, we have introduced in Ref. [26], a scaling parameter η in the function h that enforces unitarity in accordance with the Bloch model [19].

Figure 14 displays calculated scaled energy losses (Q/Z_p^2) as a function of the projectile charge Z_p for a small impact parameter ($b = 0.2$ a.u.) compared to the He 1s-shell radius ($r_0 = 0.6$ a.u.). The SCA results show up as a horizontal dashed line, since they scale with Z_p^2. The AO results for positively (open circles) and negatively charged projectiles (solid squares) are shown separately in this plot. The error bars of the AO results for positive bare ions are estimated from the numerical convergency and

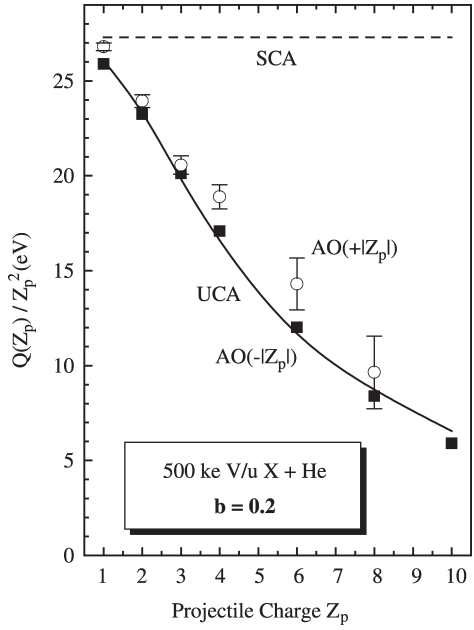

Fig. 14. Non-perturbative results for the energy loss at a small impact parameter in 500 keV/u $X^{Z_p+} + He$ collisions, compared to the values from first-order perturbation theory (SCA, dashed line). Atomic orbital (AO) coupled-channel results for positively charged particles (open circles) and for anti-nuclei (closed squares). Results using the UCA model: solid curve.

integration properties and are mainly related to the accuracy of the capture matrix elements. The uncertainties for the antiparticle energy losses are only 3%, since a large basis set of target-centered states is sufficient for accurate AO calculations. AO calculations for positive ions at 500 keV/u were performed with an explicit consideration of 10 bound projectile states, for an improved treatment of electron capture, in addition to 210 target states. It is clearly evident from this figure that the deviations between results for heavy particles and antiparticles is much smaller than the deviation from the SCA.

Thus, the even orders of an Z_p expansion, as included in the unitary convolution approximation (UCA), dominate the non-perturbative effects. The present UCA results are plotted as a solid curve. This curve lies close to the average of the AO results for particles and antiparticles. Hence, although the present UCA does not include sign-of-charge effects it perfectly describes the majority of the energy transfer processes (dominated by ionization) of fast heavy particles at small impact parameters.

7. WHAT HAVE WE LEARNED FROM COUPLED-CHANNEL CALCULATIONS

Virtually all non-trivial collision theories are based on the impact-parameter method and on the independent-electron model, where one active electron moves under the influence of the combined field of the nuclei and the remaining electrons frozen in their initial state. Most theories additionally rely on much more serious assumptions as, e.g., adiabatic or sudden electronic transitions, perturbative or even classical projectile/electron interactions. All these assumptions are circumvented in this work by solving the time-dependent Schrödinger equation numerically exact using the atomic-orbital coupled-channel (AO) method. This non-perturbative method provides full information of the basic single-electron mechanisms such as target excitation and ionization, electron capture and projectile excitation and ionization. Since the complex populations amplitudes are available for all important states as a function of time at any given impact parameter, practically all experimentally observable quantities may be computed.

Huge-basis set calculations have been performed with hundreds of states, including bound atomic orbitals of the target and target-centered continuum wave-packets. If necessary bound projectile states are included as well. These calculations involve solutions of the Schrödinger equation for each impact parameter and for all important projectile charge-states weighted with the corresponding charge-state fraction. Thus, not only the screened target potential (in most cases a self-consistent Hartree–Fock–Slater potential) but also screened projectile potentials have to be considered.

In recent years, the model was applied to the light atomic targets H and He and a few selected solids (C, Al and Si) for projectile nuclear charges between -10 and $+10$. Total cross section, mean energy transfers, energy-loss and straggling cross sections, electron energy and angular distributions, and projectile-angle dependent energy-loss spectra have been computed with the AO model and compared to experimental results. As shown in this work, also a treatment of multiphoton ionization beyond perturbation theory is possible with the same model. Here we have found numerical limitations concerning the laser power-density, pulse-width and frequency.

So far we found no serious limitations for the treatment of collision processes concerning the projectile nuclear charge (comparable to the case of high laser power-densities). At low projectile velocities, however, the calculations require the use of basis sets with extremely dense energy grids. High orders of the perturbation series often dominate the ionization probabilities for this case and high computation times are thus needed. This situation is similar to the case of long laser pulses with low frequencies and intermediate to high power densities.

We have applied our code to kinetic projectile energies of up to a few hundred keV per nucleon. In most cases good agreement with experimental

data was found. The remaining cases could be traced back to a breakdown of the independent electron model. For light targets, di-electronic transitions and for heavy targets collective dynamic screening effects modify the mean electronic motion and lead to uncertainties of up to about 20% for the electronic energy loss. Especially for slow heavy particles in the molecular-orbital regime, electron-exchange and dynamic mean-field effects are important and have to be incorporated in the treatment. A small impact parameters a simple united-atom treatment is usually sufficient, but a more general solution would be a time-dependent Hartree–Fock (TDHF) treatment as it is often applied to nuclear collision processes.

Another problematic point appears in the treatment of electron loss due to heavy (neutral) targets. In this case, unrealistic capture processes come into play where the projectile electron is transferred into populated bound target states. In principle, this problem may be circumvented by using the multielectron anti-symmetrization method, where the Pauli exclusion principle is enforced for the transitions amplitudes. Thus, an explicit and time-consuming treatment of these occupied bound states would then be necessary.

In most cases, however, for atoms, insulators or inner shells of conductors accurate stopping cross sections may be computed (including excitation, ionization and electron capture) using the AO coupled-channel method. This is a time-consuming task, since it has to be done for each subshell, each impact parameter and each projectile charge-state separately. On the other hand, it provides full information about all single-electron transitions. In general, at low projectile energies target excitation or electron capture give rise to the largest transition probabilities and cross sections. Since, quasi-molecular effects are important, the impact-parameter dependence may even show an oscillating behavior. At high projectile velocities (compared to the mean electron-orbital velocity) ionization dominates the electronic energy loss and the energy transfer is typically a smoothly decaying function of the impact parameter.

The AO results may also be used for benchmark tests of simpler models. In this context we have also checked a simple non-perturbative model, the UCA. This model includes the main features of fast heavy-ion stopping, as is shown by comparison with large-scale AO results for the impact-parameter dependent electronic energy transfer. The computation of the energy loss within the UCA is much simpler and by many orders of magnitude faster than the full numerical solution of the time-dependent Schrödinger equation.

ACKNOWLEDGEMENTS

Part of this work (the photoionization section) was performed in collaboration with Melanie Roth (HMI, Berlin). We would also like to

acknowledge R.C. Fadanelli for the final revision of the manuscript. This work was partially supported by CAPES-PROBRAL Project 121/00, by CNPq and by the Alexander-von-Humboldt foundation.

REFERENCES

[1] D. R. Bates and G. Griffing, *Proc. Phys. Soc.*, 1953, **A66**, 961.
[2] E. J. McGuire, *Phys. Rev. A*, 1971, **3**, 267; E. J. McGuire, *Phys. Rev. A*, 1983, **28**, 2096; E. J. McGuire, *Phys. Rev. A*, 1998, **57**, 2758.
[3] H. Bethe, *Ann. Phys.*, 1930, **5**, 325.
[4] N. M. Kabachnik, V. N. Kondratev and O. V. Chumanova, *Phys. Status Solidi (b)*, 1988, **145**, 103.
[5] P. D. Fainstein, V. H. Ponce and A. E. Martinez, *Phys. Rev. A*, 1993, **47**, 3055.
[6] R. E. Olson, *Radiat. Effects Defects Solids*, 1989, **110**, 1.
[7] P. L. Grande and G. Schiwietz, *J. Phys. B: At. Mol. Opt. Phys.*, 1995, **28**, 425.
[8] G. Maynard, K. Katsonis, C. Deutsch, *et al*., *Nucl. Instrum. Methods*, 2001, **A464**, 86; G. Maynard, G. Zwicknagel, C. Deutsch, *et al*., *Phys. Rev. A*, 2001, **63**, 2903.
[9] R. Cabrera-Trujillo, Y. Ohrn, J. R. Sabin and E. Deumens, *Phys. Rev. A*, 2002, **65**, 024901; R. Cabrera-Trujillo, Y. Ohrn, E. Deumens and J. R. Sabin, *Phys. Rev. A*, 2000, **62**, 052714.
[10] G. Schiwietz, *Phys. Rev. A*, 1990, **42**, 296.
[11] P. L. Grande and G. Schiwietz, *Phys. Rev. A*, 1991, **44**, 2984.
[12] G. Schiwietz and P. L. Grande, *Nucl. Instrum. Methods*, 1992, **B69**, 10; P. L. Grande and G. Schiwietz, *Phys. Rev. A*, 1993, **47**, 1119.
[13] P. L. Grande and G. Schiwietz, *Nucl. Instrum. Methods*, 1997, **B132**, 264.
[14] N. R. Arista, *Nucl. Instrum. Methods*, 2002, **B195**, 91; A. F. Lifschitz and N. R. Arista, *Phys. Rev. A*, 1998, **57**, 200; J. E. Valdes, P. Vargas and N. R. Arista, *Phys. Rev. A*, 1997, **56**, 4781.
[15] I. Campillo, J. M. Pitarke and A. G. Eguiluz, *Phys. Rev. B*, 1998, **58**, 10307.
[16] J. J. Dorado and F. Flores, *Phys. Rev. A*, 1993, **47**, 3092.
[17] P. M. Echenique, R. M. Nieminem and R. H. Ritchie, *Solid State Commun.*, 1981, **37**, 779; P. M. Echenique, R. M. Nieminem, J. C. Ashley and R. H. Ritchie, *Phys. Rev. A*, 1986, **33**, 897.
[18] N. Bohr, *Phil. Mag.*, 1913, **25**, 10; N. Bohr, *Phys. Rev.*, 1941, **59**, 270.
[19] F. Bloch, *Ann. Physik*, 1933, **16**, 285.
[20] P. Sigmund and U. Haagerup, *Phys. Rev. A*, 1986, **34**, 892; H. H. Mikkelsen and P. Sigmund, *Phys. Rev. A*, 1989, **40**, 101; H. H. Mikkelsen, *Nucl. Instrum. Methods*, 1991, **B58**, 136.
[21] P. Sigmund and A. Schinner, *Eur. Phys. J. D.*, 2000, **12**, 425; P. Sigmund and A. Schinner, *Phys. Scripta*, 2001, **T92**, 222.
[22] J. H. R. dos Santos, P. L. Grande, M. Behar, H. Boudinov and G. Schiwietz, *Phys. Rev. B*, 1997, **55**, 4332.
[23] P. L. Grande and G. Schiwietz, *Nucl. Instrum. Methods*, 1998, **B136–138**, 125.
[24] P. L. Grande, A. Hentz, G. Schiwietz, W. H. Schulte, B. W. Busch, D. Starodub and T. Gustafsson, *Phys. Rev. B*, 2003.
[25] P. L. Grande and G. Schiwietz, *Phys. Rev. A*, 1998, **58**, 3796.
[26] G. Schiwietz and P. L. Grande, *Nucl. Instrum. Methods*, 1999, **B153**, 1.
[27] ISL Annual Report, HMI-B587, p. 20, 2001.
[28] J. Bang and J. M. Hansteen, *Kgl. Dan. Vidensk. Selsk. Mat. Fys. Medd.*, 1959, **31** (13); L. Wilets and S. J. Wallace, *Phys. Rev.*, 1968, **169**, 84; M. R. Flannery and K. J. MacCann, *Phys. Rev. A*, 1973, **8**, 2915.

[29] G. Baur, M. Pauli and D. Trautmann, *Nucl. Phys.*, 1974, **A211**, 333.
[30] J. H. McGuire and L. Weaver, *Phys. Rev. A*, 1977, **16**, 41.
[31] L. Kocbach, J. U. Andersen, E. Laegsgaard and M. Lund, in *Proceedings of the 10th International Conference on the Physics of Electronic and Atomic Collisions*, Paris, (ed. G. Watel), North-Holland, Amsterdam, 1977, p. 42.
[32] M. Kleber and K. Unterseer, *Z. Phys. A*, 1979, **292**, 311.
[33] F. Rösel, D. Trautmann and G. Bauer, *Nucl. Instrum. Methods*, 1982, **192**, 43.
[34] L. Wilets and S. J. Wallace, *Phys. Rev.*, 1968, **169**, 84; R. Mc Carrol and A. Salin, *J. Phys.*, 1968, **B1**, 163; M. R. C. Mc Dowell and J. P. Coleman, *Introduction to the Theory of Ion–Atom Collisions*, North-Holland, Amsterdam, 1970.
[35] S. T. Manson, L. H. Toburen, D. H. Madison and N. Stolterfoht, *Phys. Rev. A*, 1975, **12**, 60.
[36] M. Inokuti, *Rev. Mod. Phys.*, 1971, **43**, 297.
[37] F. Herman and S. Skillmann, *Atomic Structure Calculations*, Prentice-Hall, Englewood Cliffs, NJ, 1963.
[38] J. H. McGuire, N. Stolterfoht and P. R. Simony, *Phys. Rev. A*, 1981, **24**, 97.
[39] E. C. Montenegro, W. E. Meyerhof and J. H. McGuire, *Adv. At. Mol. Opt. Phys.*, 1994, **34**, 249.
[40] A. Dalgarno and G. W. Griffing, *Proc. R. Soc.*, 1955, **A232**, 423.
[41] A. Arnau, *Nucl. Instrum. Methods*, 1996, **B115**, 2.
[42] R. D. Cowan, *The Theory of Atomic Structure and Spectra*, University of California Press, London, 1981.
[43] U. Heinz, W. Greiner and B. Müller, *Phys. Rev. A*, 1979, **20**, 130.
[44] J. F. Reading, T. Bronk, A. L. Ford, L. A. Wehrman and K. A. Hall, *J. Phys. B: At. Mol. Opt. Phys.*, 1997, **30**, L189.
[45] A. Messiah, *Quantum Mechanics*, North-Holland/Interscience, Amsterdam/New York, 1963, Vol. 2.
[46] M. Abramowitz and I. Stegun, *Handbook of Mathematical Functions*, Dover, New York, 1970.
[47] A. Salin, private communication.
[48] W. Fritsch and C. D. Lin, *J. Phys. B*, 1982, **15**, 1225; W. Fritsch and C. D. Lin, *Phys. Rev. A*, 1983, **27**, 3361.
[49] Fritsch, private communication.
[50] J. F. Reading, T. Bronk, A. L. Ford, L. A. Wehrman and K. A. Hall, *J. Phys. B: At. Mol. Opt. Phys.*, 1997, **30**, L189.
[51] H. Knudsen, U. Mikkelsen, K. Kirsebom, S. P. Moeller, E. Uggerhoef, J. Slevin, M. Charlton and E. Morenzoni, *Phys. Rev. Lett.*, 1995, **74**, 4627.
[52] G. Schiwietz, U. Wille, R. Diez Muiño, P. D. Fainstein and P. L. Grande, *J. Phys. B: At. Mol. Opt. Phys.*, 1996, **29**, 307.
[53] F. Ziegler, J. P. Biersack and U. Littmark, *The Stopping and Range of Ions in Solids*, Pergamon Press, London, 1985, ISBN 0-08-021603.
[54] P. L. Grande, F. C. Zawislak, D. Fink and M. Behar, *Nucl. Instrum. Methods*, 1991, **B61**, 282.
[55] H. Ryufuku and T. Watanabe, *Phys. Rev. A*, 1978, **18**, 2005; H. Ryufuku and T. Watanabe, *Phys. Rev. A*, 1979, **19**, 1538; U. Wille, *J. Phys. B: At. Mol. Phys.*, 1983, **16**, L275.
[56] L. L. Balashova, N. M. Kabachnik and V. N. Kondratev, *Phys. Status Solidi (b)*, 1991, **161**, 113.
[57] H. H. Mikkelsen and H. Flyvbjerg, *Phys. Rev. A*, 1990, **42**, 3962.
[58] D. Charalambidis, D. Xenakis, C. J. G. J. Uiterwaal, P. Maragakis, J. Zhang, H. Schröder, O. Faucher and P. Lampropoulos, *J. Phys. B: At. Mol. Opt. Phys.*, 1997, **30**, 1467.
Q1 [59] F. H. M. Faisal, Plenum Press, London, 1987.
[60] H. J. Lüdde, A. Henne, A. Salin, A. Toepfer and R. Dreizler, *J. Phys. B: At. Mol. Opt. Phys.*, 1993, **26**, 2667.

[61] G. Schiwietz, P. L. Grande, C. Auth, H. Winter and A. Salin, *Phys. Rev. Lett.*, 1994, **14**, 2159.
[62] C. Auth and H. Winter, *Phys. Lett.*, 1993, **A176**, 3055.
[63] S. K. Allison, *Rev. Mod. Phys.*, 1958, **30**, 1137.
[64] H. K. Reynolds, D. N. F. Dunbar, W. A. Wenzel and W. Whaling, *Phys. Rev.*, 1953, **92**, 742.
[65] J. A. Phillips, *Phys. Rev.*, 1953, **90**, 532, d and t projectiles were used for incident energies below 40 keV.
[66] P. K. Weyl, *Phys. Rev.*, 1953, **91**, 289.
[67] J. T. Park and E. J. Zimmermann, *Phys. Rev.*, 1963, **131**, 1611.
[68] F. Besenbacher, H. H. Andersen, P. Hvelplund and H. Knudsen, *Mat. Fys. Medd. Dan. Vid. Selsk.*, 1979, **40** (3).
[69] R. Golser and D. Semrad, *Phys. Rev. Lett.*, 1991, **66**, 1831.
[70] D. Niemann, P. Oberschachtsiek, S. Kalbitzer and H. P. Zeindl, *Nucl. Instrum. Methods*, 1993, **B80/81**, 37.
[71] R. J. Petty and G. Dearnaley, *Phys. Lett.*, 1974, **50A**, 273.
[72] H. S. Jin and W. M. Gibson, *Nucl. Instrum. Methods*, 1986, **B13**, 76.

Author Queries

JOB NUMBER: 4739

Title Ionization and Energy Loss Beyond Perturbation Theory

Q1 Please provide more details in Ref. [59].